Relaxation dynamics of spin-$\frac{3}{2}$ silicon vacancies in 4*H*-SiC

A. J. Ramsay [1] and A. Rossi [2,3]

[1]*Hitachi Cambridge Laboratory, Hitachi Europe Ltd., Cambridge CB3 0HE, United Kingdom*

[2]*Department of Physics, SUPA, University of Strathclyde, Glasgow G4 0NG, United Kingdom*

[3]*National Physical Laboratory, Hampton Road, Teddington TW11 0LW, United Kingdom*

(Received 20 December 2019; revised manuscript received 27 March 2020; accepted 27 March 2020; published 17 April 2020)

Room-temperature optically detected magnetic resonance experiments on spin-$\frac{3}{2}$ silicon vacancies in 4*H*-SiC are reported. The $m_s = +\frac{1}{2} \leftrightarrow -\frac{1}{2}$ transition is accessed using a two-microwave-frequency excitation protocol. The ratio of the Rabi frequencies of the $+\frac{3}{2} \leftrightarrow +\frac{1}{2}$ and $+\frac{1}{2} \leftrightarrow -\frac{1}{2}$ transitions is measured to be (0.901 ± 0.013). The deviation from $\sqrt{3}/2$ is attributed to small difference in g factor for different magnetic dipole transitions. Whereas a spin-$\frac{1}{2}$ system is characterized by a single-spin lifetime T_1, we experimentally demonstrate that the spin-$\frac{3}{2}$ system has three distinct relaxation modes that can be preferentially excited and detected. The measured relaxation times are $(0.41 \pm 0.02)T_{\text{slow}} = T_d = (3.3 \pm 0.5)T_{\text{fast}}$. This differs from the values of $T_p/3 = T_d = 2T_f$ expected for pure dipole (T_p), quadrupole (T_d), and octupole (T_f) relaxation modes, respectively, and implies admixing of the slow dipole and fast octupole relaxation modes.

DOI: 10.1103/PhysRevB.101.165307

I. INTRODUCTION

The density matrix of a qubit is often decomposed into the identity and three Pauli spin-$\frac{1}{2}$ matrices. The resulting Bloch vector provides an intuitive picture of the spin-$\frac{1}{2}$ dynamics, and the populations relax with a single-spin lifetime termed T_1. A spin-$\frac{3}{2}$ system has four states, and is described by a 4×4 density matrix. By extension, the relaxation of the four spin populations is described by three relaxation modes, characterized by three time constants. Furthermore, the 4×4 density matrix can be represented by a multipole expansion of the identity, $\times 3$ dipole ($\mathcal{P}$), $\times 5$ quadrupole ($\mathcal{D}$), and $\times 7$ octupole ($\mathcal{F}$) modes providing a more intuitive representation of the spin-$\frac{3}{2}$ density matrix [1]. This representation has advantages for understanding the spin-relaxation processes of $S = \frac{3}{2}$. For example, a dipolelike perturbation does not mix different order poles fixing the spin-relaxation times such that $T_p/3 = T_d = 2T_f$, as recently discussed theoretically in the case of a fluctuating magnetic field acting on a silicon vacancy in SiC [2,3]. However, as we will demonstrate, this is not the case in practice.

An accessible spin-$\frac{3}{2}$ system for testing this prediction is the V2 silicon vacancy in 4*H*-SiC [2,4,5]. Recently, a number of groups have demonstrated that defects in SiC have optically accessible spins with coherence times on a par with diamond [5,6]. Unlike diamond, the manufacturing of SiC electronic devices is advanced. For example, *n*- and *p*-type doping can be routinely achieved and good quality SiO_2 films can be deposited or grown on the surface, enabling CMOS processing. Due to the large breakdown voltages of SiC diodes and transistors, SiC devices are increasingly used in power electronic applications relevant to electric trains, cars, and power transmission. As such, rapid improvement in materials and device quality is to be expected, and there is growing interest in SiC for quantum devices [7–11].

Here, we report room-temperature optically detected magnetic resonance (ODMR) experiments on an ensemble of silicon vacancies in 4*H*-SiC. By using a two-microwave-frequency setup, the $+\frac{1}{2} \leftrightarrow -\frac{1}{2}$ transition can be detected optically [2,12,13]. Rabi oscillations of all three magnetic-dipole-allowed transitions are measured. The ratio of the Rabi frequencies is compared to the value of $\sqrt{3}/2$, expected for S_x matrix. A small difference in the in-plane g factor for the $\pm\frac{3}{2} \leftrightarrow \pm\frac{1}{2}$ and $+\frac{1}{2} \leftrightarrow -\frac{1}{2}$ transitions is measured. In a typical T_1 measurement [2], a laser pulse initializes and detects the quadrupole state that decays exponentially with a time constant of $T_d = 131\ \mu$s. Here we use pulse sequences with two microwave frequencies that preferentially generate and detect the octupole and dipole states, and then measure their relaxation dynamics. The relaxation of the spin-$\frac{3}{2}$ is found to comprise of three modes with three time constants. The symmetry between exciting $\pm\frac{3}{2} \leftrightarrow \pm\frac{1}{2}$ transitions implies that one of the relaxation modes is the quadrupole. However, the fast relaxation mode decays much faster than expected for a pure octupole relaxation mode, with $T_{\text{fast}} < T_d/2$. Therefore, contrary to expectations of Ref. [2], the dipole and octupole relaxation modes are admixed due to a relatively fast relaxation between $+\frac{1}{2} \leftrightarrow -\frac{1}{2}$ states.

II. EXPERIMENTAL DETAILS

The silicon vacancy is a point defect due to a missing silicon atom. In 4*H*-SiC, there are two species of defect due to two inequivalent lattice sites with near-hexagonal or cubic point symmetry [14,15]. Here we nominally study an ensemble of V2 defects with a zero phonon line at 916 nm at low temperature since it can be detected in ODMR at room temperature [4,5]. The V2 is associated with the cubic k site [16], and a zero-field fine-structure splitting of 70 MHz.

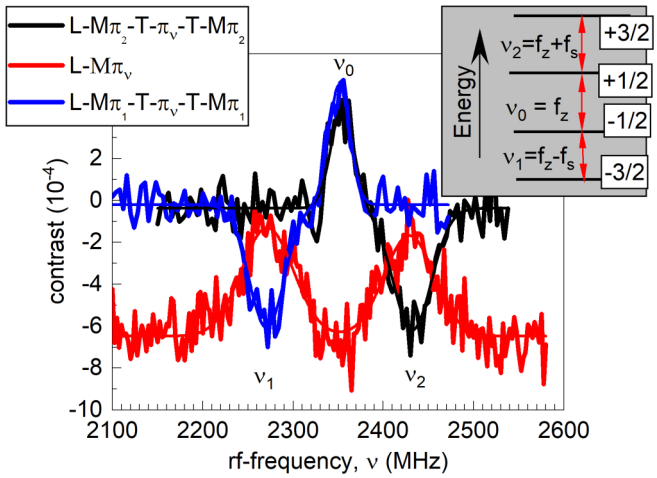

FIG. 1. (Inset) Energy-level diagram of $S = \frac{3}{2}$ ground state with dc B field applied along c axis. The magnetic-dipole-allowed transitions are labeled ν_a. (Main panel) (Red) Single-frequency ODMR spectra. ODMR is only sensitive to population difference between $\pm\frac{3}{2}$ and $\pm\frac{1}{2}$ states, hence, the ν_0 transition is not observed. (Black/blue) Two-frequency ODMR spectra, showing change in signal due to π pulse inserted between two π pulses tuned to ν_1 (ν_2) transitions. The ν_0 transition is now observed. $2f_s = 158 \pm 4$ MHz, $f_z = 2350 \pm 2$ MHz. The offset is arbitrary.

The sample used was purchased from CREE. The substrate is n-type LPBD. There is 30-μm epilayer that is slightly n type (3×10^{15} cm^{-3}). Due to the n-type substrate, the samples have a dark yellow color. The experiments were made using native defects of the epilayer.

The silicon vacancy is optically polarized along the c axis. To improve optical collection efficiency by a factor of 5–7, the chip is cleaved and mounted on its side to collect light perpendicular to the c axis [5]. The 785-nm pump laser is chopped with an acousto-optic modulator and coupled into a home-built microscope with a dichroic mirror. The laser (14 mW) is focused on the side of the chip with a NA = 0.75 air objective to a $\approx$1 μm spot size. The photoluminescence is fiber coupled to a Si-APD module. The count rate is set to an optimum of about 3 MHz. Typically, 10^8 counts are accumulated to achieve a standard deviation of 10^{-4}. This results in long integration times. A typical trace in Fig. 1 takes about 2 h to measure, and Fig. 3(d) took about 2 weeks. The ac B field is applied along the laser axis, perpendicular to the c axis, using a loop antenna fashioned from a coaxial cable, and a dc B field nominally along the c axis is applied by positioning a permanent magnet.

III. TWO-TONE ODMR SPECTRA

The inset of Fig. 1 shows the energy-level diagram of the spin-$\frac{3}{2}$ ground state in a strong magnetic field of approximately 84 mT applied along the c axis. To locate the transitions ν_1 and ν_2, a single-frequency ODMR spectrum is measured. This is done by applying a $\tau_L = 3.8$ μs nonresonant laser pulse to generate a net spin in the $\pm\frac{3}{2}$ states [5]. Then, a 30-ns radio-frequency (rf) π pulse is applied, if this is resonant with either the ν_1 or ν_2 transition the $m_s = -\frac{1}{2}$ ($m_s = +\frac{1}{2}$) state is populated resulting in a slightly increased fluorescence when a second laser pulse is applied. A lock-in measurement comparing signals with and without the rf pulse is used. Two peaks are observed. We note that the frequency splitting $2f_s = 158 \pm 4$ MHz is larger than the 140 MHz expected for $V2_{Si}^-$ defects in 4H-SiC. We do not attribute this to a misalignment of the magnetic field with respect to the c axis since this would reduce the splitting. We note that in Ref. [17], a slightly larger than expected splitting was also reported for single V2-related defect. Most likely, the larger than expected splitting here is due to an ensemble of silicon vacancies perturbed by nearby defects. There are a number of $S = \frac{3}{2}$ complexes associated with a negative silicon vacancy, with a nearby defect along the c axis with various splittings [18]. In particular, the R2 complex is a close match with a splitting of $4D = 157.6$ MHz [18].

To detect the ν_0 transition, a two-frequency pulse sequence $L - M\pi_{1,2} - T - \pi_\nu - T - M\pi_{1,2}$ is used. The notation summarizes the pulse sequence with time going left to right. L indicates the laser pulse for initialization and detection. π_a indicates a π pulse on the a transition, T a time delay. For lock-in detection, the experiment alternates between two slightly different pulse sequences at half the repetition rate. M precedes a pulse that is switched on and off at the repetition rate. Here, the first π_2 pulse generates a population inversion between the $m_s = +\frac{1}{2}$ and $-\frac{1}{2}$ states, that can be driven by a π_0 pulse. The final π_2 pulse swaps the populations of the $+\frac{3}{2}$ and $+\frac{1}{2}$ states projecting a population between $\pm\frac{1}{2}$ states into the measurement basis. The two-frequency spectra are displayed in Fig. 1. An additional peak corresponding to ν_0 is observed confirming that the ground state is spin $\frac{3}{2}$. A dip at the $\nu_{1,2}$ transition is observed since the lock-in compares the signals generated by sequences with three consecutive $\pi_{1,2}$ and one $\pi_{1,2}$ pulse, respectively. This is narrower than the single-frequency peak, due to a spectral hole burning effect, whereby the prepulse selects a subset of defects to be probed by the π_ν pulse [2,12]. The $\nu_{2,1}$ peaks are absent since the $\pi_{1,2}$ and $\pi_{2,1}$ pulses interact with different spin states, and the independent unmodulated signal generated by frequency scanned π_ν pulse is canceled.

IV. RABI FREQUENCIES OF SPIN $\frac{3}{2}$

A key property of spin-$\frac{3}{2}$ system is that the Rabi frequencies of the $\nu_{1,2}$ and ν_0 transitions should have a ratio of $\sqrt{3}/2$ due to the ratio of the relevant elements of the $S = \frac{3}{2}$ S_x matrix. Rabi oscillation measurements are made for all three transitions (see Fig. 2). Since the prepulse selects a subset of defects, the damping of the ν_0 Rabi oscillation due to ensemble broadening is reduced. To measure the ratio of the Rabi frequencies, Rabi oscillations are measured as a function of rf power at a frequency of 2340.09 MHz by tuning the resonances with the external magnetic field. This eliminates changes in the applied power due to the frequency response of the loop antenna. The Rabi frequencies are extracted by fit to a model that accounts for the ensemble broadening [the red lines in Fig. 2(a) give example fits]. Figure 2(b) displays a plot of Rabi frequency squared of the ν_2 and ν_0 transitions. This plot eliminates effects of saturation of the power applied at

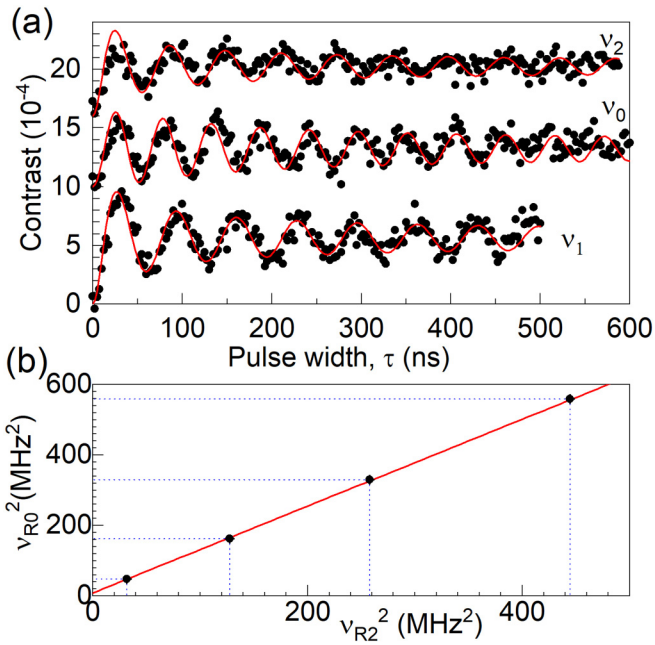

FIG. 2. (a) Rabi oscillations of all three magnetic-dipole-allowed transitions. (b) Plot of ν_{R0}^2 versus ν_{R2}^2 Rabi frequencies squared, measured at rf frequency $\nu_{\rm rf} = 2340.9$ MHz for various rf powers. Data offset for clarity.

the loop antenna, and the intercept accounts for contributions to the effective Rabi frequency due to small detunings or dephasing. The gradient gives R^{-2}, where R is the ratio of the ν_{R2}/ν_{R0} Rabi frequencies, with $R = 0.901^{+0.009}_{-0.013}$. This is larger than the value of $\sqrt{3}/2$ expected for an isotropic $S = \frac{3}{2}$ system.

The deviation in the ratio R from $\sqrt{3}/2$ can be interpreted as a slight difference in the g factors of the two transitions. We define an anisotropic g-factor tensor $g_{ij,k}$, such that the Zeeman Hamiltonian is $H_Z = \mu_B g_{ij,k} S_{ij,k} B_k$. The in-plane ac B field is aligned along x, and $R = \frac{\sqrt{3}}{2}\frac{g_{+3/2\leftrightarrow+1/2,x}}{g_{+1/2\leftrightarrow-1/2,x}}$. Then, following notation of Ref. [19], we further define a deviation from $g_{ij,x} = g_\perp$, such that $g_{+3/2\leftrightarrow+1/2,x} = g_\perp + g_{2\perp}$, and $g_{+1/2\leftrightarrow-1/2,x} = g_\perp - g_{2\perp}$, and deduce $\frac{g_{2\perp}}{g_\perp} = +0.019^{+0.005}_{-0.007}$. This is consistent with value of $\frac{g_{2\perp}}{g_\perp} = 0.0 \pm 0.05$ reported in Ref. [19]. For further details of the analysis, see Appendix A.

V. SPIN-RELAXATION MODES

The spin-relaxation dynamics of the four-state $S = \frac{3}{2}$ system can be described by the matrix $\mathcal{R}$, such that $\dot{\rho}_{ii} = -\mathcal{R}_{ij}\rho_{jj}$, where the diagonal of the density matrix ρ_{jj} represents the populations in the $m_s = (+\frac{3}{2}, +\frac{1}{2}, -\frac{1}{2}, -\frac{3}{2})$ states, respectively. If we assume that only $\Delta m_s = \pm 1$ transitions are allowed, the relaxation matrix has the form

$$\mathcal{R} = \begin{pmatrix} \gamma_1 & -\gamma_1 & 0 & 0 \\ -\gamma & \gamma_1+\gamma_2 & -\gamma_2 & 0 \\ 0 & -\gamma_2 & \gamma_3+\gamma_2 & -\gamma_3 \\ 0 & 0 & -\gamma_3 & \gamma_3 \end{pmatrix}. \quad (1)$$

Therefore, the spin-relaxation dynamics can be decomposed into four eigenmodes. The first is the identity ($\rho = \mathbb{1}$) with a decay rate of zero. In the case where $\gamma_1 = \gamma_3 = \gamma/2$, the eigenvalues of $\mathcal{R}$ are

$$\frac{1}{T_d} = \gamma,$$
$$\frac{1}{T_{\rm fast,slow}} = \frac{\gamma}{2} + \gamma_2 \pm \frac{1}{2}\sqrt{\gamma^2 + 4\gamma_2^2}. \quad (2)$$

In the special case considered in Ref. [2] where an effective magnetic field gives rise to fluctuations with dipolelike symmetry, $\gamma_2 = 2\gamma/3$, and the eigenmodes are the pure dipole [$\mathcal{P}_0 = (3, 1, -1, -3)/\sqrt{20}$], quadrupole [$\mathcal{D}_0 = (1, -1, -1, 1)/2$], and octupole [$\mathcal{F}_0 = (1, -3, 3, -1)/\sqrt{20}$] modes with relaxation times $T_p = 3T_d = 6T_f$. If, however, the fluctuations have a component with quadrupolelike symmetry, then $\gamma_2 \neq 2\gamma/3$, and admixing of the dipole and octupole relaxation modes occurs.

To test this picture, a series of measurements are made to preferentially generate and detect the dipole, quadrupole, and octupole modes, and measure their relaxation rates. Figure 3(a) shows the relaxation of a pure quadrupole mode using the pulse sequence ($L - T - M\pi_1 - L$) to initialize in $\mathcal{D}_0$, and then make a projective measurement at time delay T. This is the usual protocol used to measure the "T_1" time [2,20]. Consistent with previous reports, a single exponential decay is observed. A similar measurement is made on the ν_2 transition [see Fig. 3(b)]. Decay times of $T_{d\nu_1} = 128 \pm 13$ μs and $T_{d\nu_2} = 133 \pm 11$ μs are measured; these are the same within experimental error. This implies a symmetry between the ν_1 and ν_2 transitions, such that $\gamma_1 \approx \gamma_3$, and confirms that the quadrupole is an eigenmode of the relaxation matrix $\mathcal{R}$, with $T_d = 131 \pm 8$ μs. This is toward the short end of the T_1 values reported for $V2^-_{\rm Si}$ in natural 4H-SiC. Together with the relatively short spin-echo times $T_2(SE) < 2$ μs, this suggests the defect density of the sample is relatively high $N_V \sim 10^{16}$ cm^{-3} in this sample [20,21], or the relatively high background n-type doping ($n = 3 \times 10^{15}$ cm^{-3}) may reduce the stability of the defects charge state.

If the dipole and octupole relaxation modes are uncoupled, the pulse sequences [$L - \pi_1 - T - (M\pi_0)\pi_1 - L$] and [$L - \pi_1\pi_0 - T - (M\pi_0)\pi_1 - L$], as used for Figs. 3(c) and 3(d), should generate a mostly octupole signal $S(T) \propto +0.2e^{-T/T_p} - 1.2e^{-T/T_f}$ and a mixed $S(T) \propto +0.5e^{-T/T_p} + 0.5e^{-T/T_f}$, respectively. This is independent of the fidelities of the π pulses, which only affect the overall signal amplitude. These sequences are designed to cancel the quadrupole contribution, regardless of dipole/octupole admixing, and the fidelities of the π pulses.

Figure 3(c) shows the relaxation of the mostly octupole mode using the pulse sequence [$L - \pi_1 - T - (M\pi_0)\pi_1 - L$]. The offset is subtracted using a double lock-in method (see Appendix B), and since the signal crosses zero there are two relaxation components with opposite sign, as expected. A single exponential fit yields $T_{1/e} = 48 \pm 7$ μs $\approx T_f'$, this is noticeably faster than the expected value of $T_f = T_d/2 = 66$ μs. Figure 3(d) shows the relaxation of a mixture of the octupole and dipole modes using the pulse sequence [$L - \pi_1\pi_0 - T - (M\pi_0)\pi_1 - L$]. After a fast initial decay, a long

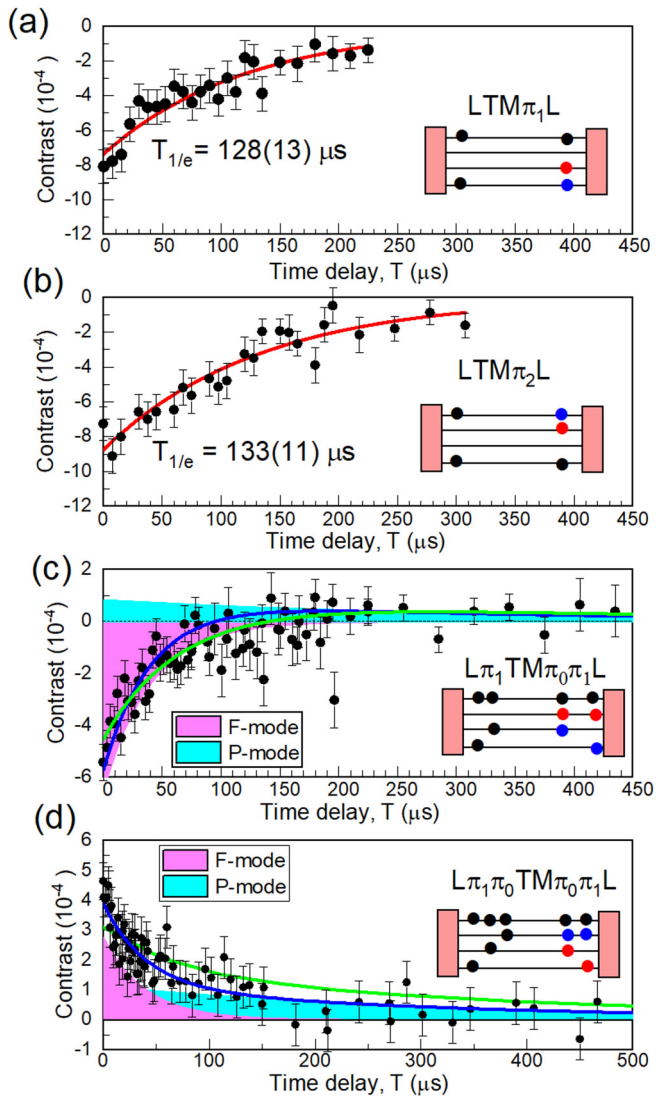

FIG. 3. Spin relaxation of qudit modes. Error bars are estimated from total counts N as error $= 1/\sqrt{N}$. (a), (b) Pure quadrupole relaxation exciting ν_1 and ν_2 transitions, respectively. (c) Mostly octupole relaxation. (d) Mixture of octupole and dipole modes. (Green) Fit with $\gamma_2 = 2\gamma/3$, where $T_p/3 = T_d = 2T_f = 131$ μs. (Blue) Fit to (d) yields $\gamma_2/\gamma = 1.33 \pm 0.27$. In (c), blue line is a calculation using $\gamma_2/\gamma = 1.33$. (Magenta/cyan) Shows the decomposition of the spin relaxation into the fast and slow decay modes. The signal offset is zero. Insets: the cartoons illustrate the pulse sequence. The four lines represent the spin states in order of energy, and the pink blocks the laser pulse. Black, red, and blue circles represent populations that are constant, and only present in case of modulated pulse ($M\pi_i$) on, and off, respectively. The cartoon depicts the case of no spin relaxation, and ideal π pulses.

tail is observed, but the ratio of the fast to slow components is larger than the expected ratio of 1:1, further demonstrating admixing of the dipole and octupole relaxation modes.

The data are modeled using Eq. (1). The initial state after laser initialization is a pure quadrupole state. The π pulses are modeled as matrix operations with a fidelity $F_0 = 0.84$ and $F_{1,2} = 0.74$ to account for imperfect inversion, and are measured by comparing to Rabi oscillation data, assuming the long time limit in the signal matches the inversion point. We note that the fidelities have a weak effect on the ratio of relaxation modes observed in Fig. 3(d) only. Otherwise, the only effect is on the overall amplitude of the signal. Following initialization of the spin, the population vector is decomposed into the relaxation eigenmodes, and following a time delay T, the projection of the read-out sequence onto quadrupole measurement basis is calculated.

To test if the relationship $T_p/3 = T_d = 2T_f$ holds, the data in Figs. 3(c) and 3(d) are fitted to the model of Eq. (1) with fixed $\gamma_2 = 2\gamma/3$ and $T_d = 131$ μs as determined from fit to Figs. 3(a) and 3(b) [see green lines of Figs. 3(c) and 3(d)]. The only fitting parameter is the amplitude. A clear deviation from the constrained model is found for Fig. 3(d), where the mixture of the P and F relaxation modes probed in the measurement are sensitive to γ_2/γ. The data of Fig. 3(d) are then fitted to model, with γ_2 as a fitting parameter yielding $\gamma_2 = (1.33 \pm 0.27)\gamma$, where the error is given by the 95% confidence level. To check consistency of the model, we then fit Fig. 3(c) with fixed $\gamma_2 = 1.33\gamma$, shown as a blue line. We then infer $T_d/T_{\text{fast}} = 3.3 \pm 0.5 \neq 2$ and $T_d/T_{\text{slow}} = 0.41^{+0.01}_{-0.02} \neq 1/3$ for the relaxation rates, with $T_{\text{fast}} = 40 \pm 6$ μs and $T_{\text{slow}} = 320^{+26}_{-22}$ μs.

VI. CONCLUSIONS

To conclude, we have presented two microwave tone optically detected magnetic resonance experiments on an ensemble of silicon vacancies in 4H-SiC, with spin $\frac{3}{2}$. These measurements provide access to all the magnetic-dipole-allowed transitions. A comparison of the Rabi frequencies for the $\pm\frac{3}{2} \leftrightarrow \pm\frac{1}{2}$ and $+\frac{1}{2} \leftrightarrow -\frac{1}{2}$ transitions allows us to measure a slightly different in-plane g factor for these transitions. The relaxation of the spin-$\frac{3}{2}$ system is shown experimentally to have three relaxation modes that can be preferentially generated and detected by choosing a particular microwave pulse sequence. This contrasts with a spin-$\frac{1}{2}$ system characterized by a single T_1 time. The spin relaxation is approximately symmetric with respect to interchange of the $\pm\frac{3}{2} \leftrightarrow \pm\frac{1}{2}$ transitions, indicating a pure quadrupole relaxation mode. Contrary to theory in Ref. [2], the decay of the short-lived octupolelike mode is faster than expected for a fluctuating in-plane B field. This indicates mixing of the octupole and dipole relaxation modes since a perturbation with dipole symmetry cannot mix different order poles. This suggests an additional fluctuation with quadrupole symmetry that mixes the dipole and octupole modes of odd order [1]. This may be the result of dipolar interactions with neighboring electron spin-$\frac{1}{2}$ defects, where the energy cost of flipping a parasitic spin-$\frac{1}{2}$ matches the Zeeman splitting of the $+\frac{1}{2} \leftrightarrow -\frac{1}{2}$ transition, and where the $\pm\frac{3}{2} \leftrightarrow \pm\frac{1}{2}$ transitions are protected by an energy mismatch due to the crystal splitting $2D \approx 70$ MHz, or may arise due to fluctuations in the crystal-field splitting D. This work demonstrates that $T_1 = T_d$ measurements do not provide complete information on spin-relaxation dynamics of spin-$\frac{3}{2}$ systems.

ACKNOWLEDGMENTS

We thank the following people for their help: J. A. Haigh and R. A. Chakalov for technical assistance; A. Shima,

K. Konishi, and K. Kobayashi of Hitachi CRL for donating the material; R. Webb of Engineering and Physical Sciences Research Council (EPSRC) ion implantation facility at University of Surrey for C-ion implantation; G. W. Morley, H. Knowles, B. Pingault, and D. Kara for advice on ODMR measurements. A.R. acknowledges financial support from UKRI's Industrial Strategy Challenge Fund through a Measurement Fellowship at the National Physical Laboratory Industrial Strategy Challenge Fund.

APPENDIX A: ANALYSIS OF RABI OSCILLATION RATIO

Because the Rabi frequency is much smaller than the splitting, $\nu_R < 25\ \text{MHz} \ll 2f_s = 158\ \text{MHz}$, and the inhomogeneous broadening dominates the damping, $\Gamma^* \gg 1/T_1, 1/T_2$ we treat the system as an ensemble of detuned ideal two-level systems. The effective Rabi frequency of the transitions is [22]

$$\nu_{R0}^2 = [g_{+1/2\leftrightarrow-1/2,x}\mu_B B_{ac}(P_{rf})]^2 + \delta_0^2, \tag{A1}$$

$$\nu_{R2}^2 = \left(g_{+3/2\leftrightarrow+1/2,x}\frac{\sqrt{3}}{2}\mu_B B_{ac}(P_{rf})\right)^2 + \delta_2^2, \tag{A2}$$

where δ_i accounts for an error in the detuning between the rf drive, and the transition i, and a tiny shift due to intrinsic dephasing. $g_{ij,k}$ is the g-factor tensor, such that the Zeeman term in the Hamiltonian is $H_Z = \mu_B g_{ij,k} S_{ij,k} B_k$, where $S_{ij,k}$ is the ij element of S_k spin-$\frac{3}{2}$ matrix. At low rf powers (P_{rf}), the ac B field $B_{\text{rf}} \propto \sqrt{P_{\text{rf}}}$. Eliminating the unknown $\mu_B B_{ac}(P_{rf})$ yields

$$\nu_{R0}^2 = \frac{2g_{+1/2\leftrightarrow-1/2}^2}{3g_{+3/2\leftrightarrow+1/2}^2}\nu_{R2}^2 + \text{constant}. \tag{A3}$$

The red lines in Fig. 2(a) show example fits used to extract the Rabi frequencies. The Rabi oscillation signal $S(T)$, an ideal two-level system with detuning, as given by Eq. (3.16) of Ref. [22], is averaged over a Gaussian distribution of detunings Δ:

$$S(T) \propto \int d\Delta \frac{\Omega_R^2}{\Lambda_R^2}\sin^2\left(\frac{\Lambda_R T}{2}\right)e^{-\frac{\Delta^2}{\Delta_0^2}}, \tag{A4}$$

where $\Omega_R = 2\pi\nu_R$ is the Rabi frequency and $\Lambda_R^2 = \Omega_R^2 + \Delta^2$ is the effective Rabi frequency. The model has three fitting parameters: the amplitude, the inhomogeneous broadening Δ_0, and the Rabi frequency ν_{Ri}. The gradient of Fig. 2(b) gives the ratio of the $R = \nu_{R2}/\nu_{R0} = 0.901 \pm 0.007 > \sqrt{3}/2$.

To evaluate systematic errors, the ratio R was calculated as a function of B-field angle, inhomogeneous broadening, and E parameter. Inhomogeneous broadening effectively dresses the Rabi frequency increasing the ratio R by $\Delta R_{\text{inhomo}} \ll +0.004$. The effects of misaligned B field and strain are computed by considering the zero B-field Hamiltonian $H_0 = D(S_z^2 - 5/4) + E(S_x^2 - S_y^2)$, where $D = 35$ MHz, and E is expected to be small [4], and an isotropic Zeeman Hamiltonian, where $g_{ijk} = g$. The ratio R increases with out-of-plane B field, with a maximum value of $R = 0.90$ at 90°. A large misalignment angle of 10° is found to increase R by $\Delta R = +0.0009$. We find that $\Delta R_E = -3.5 \times 10^{-4}\ \text{MHz}^{-1}E$. An upper limit of $|E| < 18$ MHz is given by the splitting between the ν_1 and ν_2 transitions, with $2f_s = 4\sqrt{D^2 + E^2}$ [4], yielding $|\Delta R_E| < 0.006$. Combining these errors yields $R = 0.901^{+0.009}_{-0.013}$.

APPENDIX B: DOUBLE LOCK-IN METHOD

The data collected in Sec. V use a double lock-in to achieve a stable zero offset. We use a gated APD module with 2.5 dark cps (Laser Components Count-10). The 15-ns TTL output is switched between two channels of an open-source photon counter [23] using a microwave switch (minicircuits ZWASWA-2-50DRA+). The switch slightly attenuates the TTL pulse, and it is necessary to terminate the FPGA inputs with 100Ω, rather than the usual 50Ω, to get reliable counting. An external 100-MHz clock is used (AEL9700CS) since the internal 48-MHz clock is too slow.

In general, the rf-pulse sequence alternates between sequences S1 and S2 which are directed to channels 1 and 2. At a slower frequency, typically ~0.1 Hz the order of the sequences is swapped so that S2 and S1 are directed to channels 1 and 2. By calculating $S = \frac{S1_1 - S2_2}{S1_1 + S2_2} - \frac{S2_1 - S1_2}{S2_1 + S1_2}$, a small imbalance in the detection channels $\sim 10^{-4}$ is canceled.

[1] J. R. C. van der Maarel, Thermal relaxation and coherence dynamics 3/2. I. static and fluctuating quadrupolar interactions in the multipole basis, Concepts Magn. Reson. Part A **19A**, 97 (2003).

[2] V. A. Soltamov, C. Kasper, A. V. Poshakinskiy, A. N. Anisimov, E. N. Mokhov, A. Sperlich, S. A. Tarasenko, P. G. Baranov, G. V. Astakhov, and V. Dyakonov, Excitation and coherent control of spin qudit modes in silicon carbide at room temperature, Nat. Commun. **10**, 1678 (2019).

[3] S. A. Tarasenko, A. V. Poshakinskiy, D. Simin, V. A. Soltamov, E. N. Mokhov, P. G. Baranov, V. Dyakonov, and G. V. Astakhov, Spin and optical properties of silicon vacancies in silicon carbide: A review, Phys. Status Solidi B **255**, 1700258 (2018).

[4] M. Widmann, S.-Y. Lee, T. Rendler, N. T. Son, H. Fedder, S. Paik, L.-P. Yang, Nan Zhao, Sen Yang, I. Booker, A. Denisenko, M. Jamali, S. Ali Momenzadeh, I. Gerhardt, T. Ohshima, A. Gali, E. Janzén, and J. Wrachtrup, Coherent control of single spins in silicon carbide at room temperature, Nat. Mater. **14**, 164 (2015).

[5] S. G. Carter, Ö. O. Soykal, P. Dev, S. E. Economou, and E. R. Glaser, Spin coherence and echo modulation of the silicon vacancy in 4H-SiC at room temperature, Phys. Rev. B **92**, 161202(R) (2015).

[6] W. F. Koehl, B. B. Buckley, F. J. Heremans, G. Calusine and D. D. Awschalom, Room temperature coherent control of defect spin qubits in silicon carbide, Nature (London) **479**, 84 (2011).

[7] G. Wolfowicz, S. J. Whiteley, and D. D. Awschalom, Electrometry by optical charge conversion of deep defects in 4H-SiC, Proc. Natl. Acad. Sci. USA **115**, 7879 (2018).

[8] C. P. Anderson, A. Bourassa, K. C. Miao, G. Wolfowicz, P. J. Mintun, A. L. Crook, H. Abe, J. Ul Hassan, N. T. Son, T. Ohshima, and D. D. Awschalom, Electrical and optical control

of single spins integrated in scalable semiconductor devices, Science **366**, 1225 (2019).

[9] G. Calusine, Alberto Politi, and D. D. Awschalom, Silicon carbide photonic crystal cavities with integrated color centers, Appl. Phys. Lett. **105**, 011123 (2014).

[10] J. Y. Lee, X. Lu, and Q. Lin, High-Q silicon carbide photonic-crystal cavities, Appl. Phys. Lett. **106**, 041106 (2015).

[11] A. Lohrmann, N. Iwamoto, Z. Bodrog, S. Castelletto, T. Ohshima, T. J. Karle, A. Gali, S. Prawer, J. C. McCallum, and B. C. Johnson, Single-photon emitting diode in silicon carbide, Nat. Commun. **6**, 7783 (2015).

[12] M. Niethammer, M. Widmann, S.-Y. Lee, P. Stenberg, O. Kordina, T. Ohshima, N. T. Son, E. Janzén, and J. Wrachtrup, Vector Magnetometry Using Silicon Vacancies in 4H-SiC Under Ambient Conditions, Phys. Rev. Appl. **6**, 034001 (2016).

[13] R. Nagy, M. Niethammer, M. Widmann, Y.-C. Chen, P. Udvarhelyi, C. Bonato, J. Ul Hassan, R. Karhu, I. G. Ivanov, N. Tien Son, J. R. Maze, T. Ohshima, Ö. O. Soykal, Á. Gali, S.-Y. Lee, F. Kaiser, and J. Wrachtrup, High-fidelity spin and optical control of single silicon-vacancy centres in silicon carbide, Nat. Commun. **10**, 1954 (2019).

[14] S. Castelletto, B. C. Johnson, and A. Boretti, Quantum effects in silicon carbide hold promise for novel integrated devices and sensors, Adv. Opt. Mater. **1**, 609 (2013).

[15] F. J. Heremans, C. G. Yale, and D. D. Awschalom, Wide-bandgap semiconductors for quantum technologies, Proc. IEEE **104**, 2009 (2016).

[16] V. Ivády, J. Davidsson, N. T. Son, T. Ohshima, I. A. Abrikosov, and A. Gali, Identification of Si-vacancy related room-temperature qubits in 4H silicon carbide, Phys. Rev. B **96**, 161114(R) (2017).

[17] H. B. Banks, Ö. O. Soykal, R. L. Myers-Ward, D. K. Gaskill, T. L. Reinecke, and S. G. Carter, Resonant Optical Spin Initialization and Readout of Single Silicon Vacancies in 4H-SiC, Phys. Rev. Appl. **11**, 024013 (2019).

[18] N. T. Son, P. Stenberg, V. Jakubavicius, T. Ohshima, J. Ul Hassan, and I. G. Ivanov, Ligand hyperfine interactions at silicon vacacnies in 4H-SiC, J. Phys.: Condens. Matter **31**, 195501 (2019).

[19] D. Simin, V. A. Soltamov, A. V. Poshakinskiy, A. N. Anisimov, R. A. Babunts, D. O. Tolmachev, E. N. Mokhov, M. Trupke, S. A. Tarasenko, A. Sperlich, P. G. Baranov, V. Dyakonov, and G. V. Astakhov, All-Optical dc Nanotesla Magnetometry Using Silicon Vacancy Fine Structure in Isotopically Purified Silicon Carbide, Phys. Rev. X **6**, 031014 (2016).

[20] C. Kasper, D. Klenkert, Z. Shang, D. Simin, A. Sperlich, H. Kraus, C. Schneider, S. Zhou, M. Trupke, W. Kada, T. Ohshima, V. Dyakonov, and G. V. Astakhov, Influence of irradiation on defect spin coherence in silicon carbide, arXiv:1908.06829.

[21] P. G. Brereton, D. Puent, J. Vanhoy, E. R. Glaser, and S. G. Carter, Spin coherence as a function of depth for high-density ensembles of silicon vacancies in proton-irradiated 4H-SiC, arXiv:1812.10432.

[22] L. Allen, and J. H. Eberly, *Optical Resonance and Two-level Atoms* (Wiley, New York, 1975). We use Eq. (3.16) averaged over detuning with Gaussian weight.

[23] S. Polyakov and J. Peters, Simple and inexpensive FPGA-based fast multichannel acquisition board, https://www.nist.gov/services-resources/software/simple-and-inexpensive-fpga-based-fast-multichannel-acquisition-board